May 26, 2023

The Search for Axion Like Particles (ALPs) Through B Meson Decays at the LHCb

Subrahmanya Saicharan Pemmaraju (supervised by Prof. Ulrik Egede)

An Interim Report submitted for the Master of Science

Abstract

Axions and axion-like particles (ALPs) arise naturally from particle physics theories pertaining to QCD and supersymmetry as Nambu-Goldstone bosons, which are extensions to the current Standard Model. These can explain various phenomena that are currently not well described by the Standard Model, including the absence of CP violation in the strong force. An overview of the theoretical motivation for the introduction of ALPs, along with the prospects of performing a search for these through the $B^0 \to K^{*0}a_0, a_0 \to \gamma\gamma$ decay mode at the LHCb is presented.

Contents

Acknowledgements

I would first like to expresss my heartfelt gratitude to Prof. Michael Morgan, whose timely support regarding administrative matters pertaining to my MSc candidature thus far has been instrumental in the development of this work. I would like to wholeheartedly thank my supervisor, Prof. Ulrik Egede, whose continual guidance in various aspects of this project has enabled this work to take its present form. I would also like to thank the members of the LHCb collaboration and the High Energy Physics group at Monash University, from whom I have acquired a substantial amount of exposure to both the technical, as well as phenomenological aspects of particle physics. I would particularly like to thank Dr.Tom Hadavizadeh for his assistance with developing familiarity with the LHCb simulation software. Last but not least, I would like to thank my fellow Honours and Masters students, many of whom I have had the pleasure of getting to know over the course of the two years that I have been at Monash so far.

On a personal note, I would like to extend my heartfelt gratitude to my mum, dad, and my brother Piyush, as well as those near and dear who have played a key role in keeping me motivated and sane throughout the writing process thus far. This work is dedicated to you all, for all the sacrifices you have made in order to support me during my studies. I love you all.

1   Background and Motivation

1.1   Synopsis of the Standard Model

The Standard Model of particle physics is a description of the fundamental constituents of the Universe, as well as the interactions between them. The model is composed of two main groups of particles, namely the fermions, which possess half-integer spin, and make up all of the matter within the Universe, and the gauge bosons, which are of integer spin and are responsible for mediating forces between the fermions.

The fermions can be further classified into two categories of fundamental particles known as quarks and leptons. There exist six distinct 'flavours' of quarks, which are ascribed the names up, down, charm, strange, top and bottom, denoted, u, d, c, s, t and b respectively. These are grouped into three 'generations' based on their electromagnetic charge and mass. Free quarks are never observed in nature due to a principle known as quark confinement, which mandates that these particles (and their antiparticles) should exist as bound states known as baryons and mesons (which are collectively referred to as hadrons). Quarks can interact via all of the abovementioned forces. The leptons are grouped similarly by flavour, with each generation containing a negatively charged particle and a corresponding neutrino whose electromagnetic charge is zero, and is, to a large extent, massless. The three different flavours of leptons, in ascending order of their masses, are the electron, muon, and tau, denoted e^-, μ^-, and τ^- respectively. The charged leptons can only partake in electromagnetic and weak interactions while the neutrinos can only participate in weak processes.

Figure 1: The particles of the Standard Model, grouped based on their quantum spin into gauge bosons and fermions (particles that make up all matter). The fermions are further divided into quarks and leptons which are fundamental and can partake in various interactions mediated by the gauge bosons corresponding to each of the three fundamental forces described by the model. The Higgs boson is also included and responsible for all the particles acquiring their mass. Image sourced from [1].

Three of the four fundamental forces of nature (i.e. the strong, electromagnetic, and weak forces) are accounted for in the Standard Model, as evident through the presence of vector (spin 1) gauge bosons such as the gluon (g), photon (γ), and charged W and neutral Z bosons, which mediate the aforementioned forces respectively. The model also describes a spin-0 particle, known as the Higgs boson, which, through the mechanism of spontaneous symmetry breaking, is responsible for the Standard Model particles acquiring their mass [2]. A spin-2, massless boson, known as the graviton has also been hypothesised as a mediator of the gravitational force [3]. However, there is no experimental evidence of this to date. Figure 1 provides a visual summary of the model that has been described above.

Despite providing a comprehensive description of the fundamental components of nature and the force acting between these, the Standard Model is subject to numerous limitations, the most prominent of which is its inability to account for the gravitational force [3]. Furthermore, the nature of dark matter and dark energy, which account for a large proportion of the energy density in the Universe, is not fully understood and remains an area of ongoing research. A more subtle limitation, however, pertains to a phenomenon known as CP violation and the absence of experimental evidence of this in the strong force, despite being theoretically permissible by the quantum field theory of this force, known as quantum chromodynamics (QCD) [4]. This is known as the Strong CP problem and forms the basis for motivating particles such as the axion, as well as Axion-Like Particles (ALPs), both of which are described in further detail in the sections that follow.
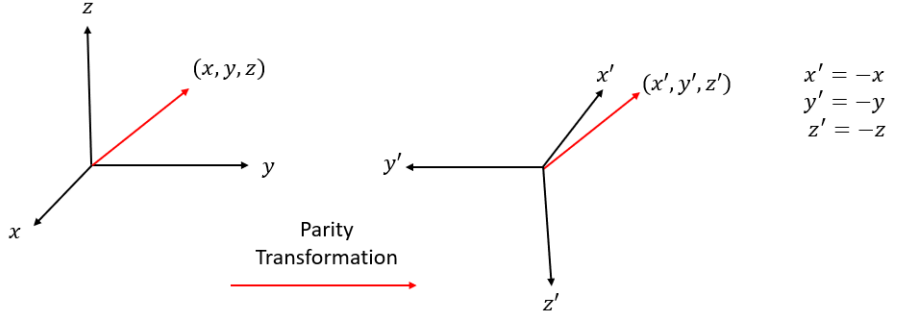
1.2 CP Violation

The principle of symmetry (i.e. the invariance of a physical system under a transformation) is significant in the study of particle physics. Two symmetries that are of particular interest are those of charge conjugation, denoted C, and parity denoted P. Charge conjugation is a transformation wherein particles within a physical system are interchanged with their antiparticles, as demonstrated in Figure 2a, while parity refers to the inversion of spatial coordinates of a physical system, as illustrated in Figure 2b below.

The combination of the abovementioned transformations is referred to as CP, and its violation is of particular interest as it provides a possible explanation for the abundance of matter over antimatter in the Universe. This link is explained by the Sakharov conditions, which state that violations of both the C and the CP symmetries, as well as that of baryon number conservation, are essential for baryogenesis [5]. CP symmetry has been observed to be preserved in electromagnetic interactions, whilst being violated in weak interactions, as demonstrated by a study of the decay of neutral kaons by Cronin and Fitch in 1964 [6]. While the theory of QCD permits the violation of this symmetry in the strong force, there is no experimental evidence of processes that violate this symmetry. This is referred to as the Strong CP problem and is essential for the theoretical motivation behind axions and ALPs [7].
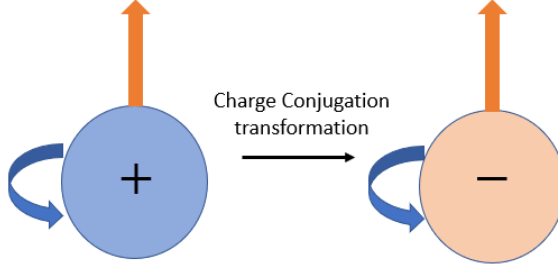
(a) The charge conjugation transformation C, which interchanges particles in a physical system with their corresponding antiparticles. Adapted from [8].

(b) An illustration of the parity transformation P, corresponding to the inversion of spatial coordinates in a physical system. Adapted from [9].

1.2.1 The Strong CP Problem

The theoretically permissible nature of CP violation in the strong force is evident within the QCD Lagrangian, which can be written in the following form [10]:

$$\mathcal{L}_{QCD} = -\frac{1}{4}G_{\mu\nu}G^{\mu\nu} - \frac{g_s^2\theta}{32\pi^2}G_{\mu\nu}\tilde{G}^{\mu\nu} + \bar{\psi}(i\gamma^\mu D_\mu - me^{i\theta'\gamma_5})\psi \tag{1}$$

where $G_{\mu\nu}G^{\mu\nu}$ represents the gluonic field strength tensor, which is the QCD equivalent of the electromagnetic field strength tensor, $F_{\mu\nu}F^{\mu\nu}$, and $\tilde{G}^{\mu\nu}$ is its dual. By construction, the operator $G_{\mu\nu}\tilde{G}^{\mu\nu}$ is CP violating, as this term preserves the parity and time-reversal symmetries, but violates the charge conjugation symmetry. The effects of the component of (1) containing this term are not experimentally observed, thereby suggesting that the term θ is infinitesimal in magnitude. One can consider a total effective angle, $\bar{\theta}$, which results from a transformation of θ, defined as

$$\bar{\theta} = \theta + Arg(\det(M_q)) \tag{2}$$

where M_q represents the quark mass matrix. This chiral transformation is essential in order to go to a physical basis by diagonalising the abovementioned quark mass matrix [11]. The absence of CP violation in the strong force suggests that $|\bar{\theta}| \approx 0$.

4

Experimental measurement of the electric dipole moment (EDM) of the neutron imposes the constraint $|\bar{\theta}| < 10^{-10}$ [12]. This is referred to as a fine-tuning problem, wherein the value of $|\bar{\theta}|$ is constrained to be as small as possible through the tuning of other parameters in order to maintain consistency with experimental observations [13].

A more elegant solution to the Strong CP problem was proposed by Peccei and Quinn in 1977 [14]. This solution involved promoting $\bar{\theta}$ to a dynamic field, thereby introducing a spatial and temporal dependence, along with an associated potential. This field is postulated to have an associated global symmetry, known as the Peccei-Quinn (PQ) symmetry. Spontaneous breaking of this symmetry mandates that $|\bar{\theta}| = 0$, thereby resolving the Strong CP Problem without the need of fine-tuning. This solution results in the introduction of the axion, which in turn leads to the motivation of Axion-Like Particles (ALPs) through the similar mechanism of spontaneous symmetry breaking, which is elaborated upon in [15].

1.3 Axions

Spontaneous breaking of the PQ symmetry described in Section 1.2.1 mandates the introduction of a light, pseudoscalar (spin-0 and odd parity) particle known as the QCD axion [14]. Axions obey a well-defined relation between their mass and coupling to Standard Model particles. For instance, the coupling constant f_A of the axion-photon coupling in one of the many axion models is inversely proportional to the mass of the axion, m_A, as demonstrated in the relationship represented in Equation 3 below [10]:

$$f_A m_A = f_{\pi^0} m_{\pi^0} \tag{3}$$

where $f_{\pi^0} = 92$ GeV^{-1} and $m_{\pi^0} = 135$ MeV correspond to the coupling strength to photons and the mass of the neutral pion, π^0, respectively.

Axions are referred to as pseudo-Nambu-Goldstone (pNG) bosons, on account of their zero spin and odd parity. There exist various axion models, which differ in their couplings to fermions and the energy scales involved. A detailed description of two of the most prominent axion models, namely the Kim-Shifman-Vainshtein-Zakharov (KSVZ), and the Dine-Fischler-Srednicki-Zhitnitsky (DFSZ) models can be obtained in [4]. Despite the variety of axion models that are proposed, these pseudoscalars are known to mix with mesons and consequently possess a model-independent coupling to photons. This coupling can be expressed through the presence of the following term in the Lagrangian [4]

$$\mathcal{L}_{a_0\gamma} = -\frac{g_{a_0\gamma}}{4} a_0 F_{\mu\nu} \tilde{F}^{\mu\nu} \tag{4}$$

where $g_{a_0\gamma}$ is the axion-photon coupling, and $F_{\mu\nu}$ and $\tilde{F}^{\mu\nu}$ represent the electromagnetic field strength tensor and its dual respectively. Other couplings of axions to fermions that are of interest for the purposes of detection include those to nucleons and electrons, the latter of which is model-dependent. Despite a wide range of searches being performed for the QCD axion employing a variety of search strategies which have been further detailed in Section (1.5), there has been no evidence of these particles to date. However, the phenomenology of axions described above serves as a motivation for the introduction of other light bosons as a consequence of other spontaneously broken symmetries at a higher energy scale [16]. These are referred to as axion-like particles, or ALPs.

1.4 Axion Like Particles (ALPs)

Spontaneous breaking of other symmetries similar to the Peccei-Quinn symmetry described in Section 1.2.1 produces particles similar to the axion, referred to as *axion-like particles* (which will henceforth be referred to as ALPs, or a_0 in decays). Unlike axions, which are expected to be very light (i.e. within the sub-eV regime), the masses of ALPs are not as constrained, thereby implying that these can be arbitrarily heavy. Furthermore, Axion-Like Particles are able to couple to pairs of gauge bosons (e.g. $\gamma\gamma, gg, HH$) as well as fermions (i.e. leptons and quarks) depending on the model being considered, and are not solely linked to the strong interaction like their counterparts [10].

ALPs are of significant importance to advancements in various fields of physics, particularly cosmology. The feeble nature of the interactions between ALPs and Standard Model particles makes them ideal dark matter candidates. In addition to this, they are believed to be able to offer an explanation of the anomalies in the energy loss of white dwarf stars [17]. Their existence can also offer an explanation of the observational hints on extra dark radiation in the primordial plasma during big bang nucleosynthesis in the form of Cosmic ALP Background (CAB) radiation [18]. Thus, a multitude of experimental methods and strategies have been employed to search for these particles, the most prominent of which include haloscope searches, Light-Shining-Through Wall (LSW) searches, and helioscope searches. These techniques, along with the constraints that they have imposed on the masses and couplings of ALPs to Standard Model particles are summarised in the sections that follow. The general search strategy and constraints imposed by collider experiments are also summarised in these sections. This, with an enhanced focus on the Large Hadron Collider beauty (LHCb) experiment, will be the primary emphasis of the remainder of this work.

1.5 Experimental Searches for Axions and ALPs

Since light pseudoscalars are theorised to naturally couple to photons, due to spin-selection rules and mass constraints, the searches for ALPs performed through cosmological and astrophysical observations, as well as those being conducted at low-energy accelerators exploit the (inverse) Primakoff effect, wherein axions are converted to photons (and vice versa) in collisions with photons, or identically with electromagnetic fields [19]. This is the case with the experimental search strategies that are summarised below, namely the Light Shining through Walls (LSW) experiments, helioscope, and haloscope searches. Further details on the nature and structure of the search techniques described below can be obtained in [20].
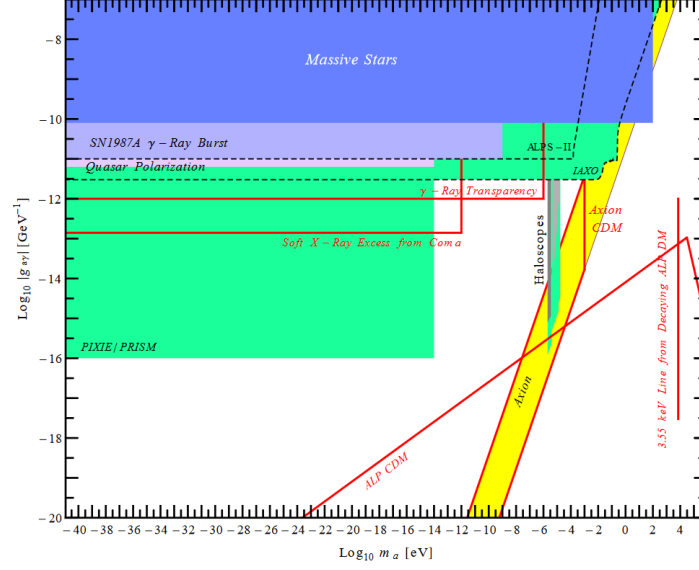
Figure 3: Log-log plot displaying the constraints imposed on the masses and coupling strengths of ALPs to photons by a variety of experiments, such as LSW, helioscope, and haloscope searches (such as ALPS-II and ADMX respectively). Of particular interest are the constraints imposed by the LSW experiments ALPS-II, as well as the helioscope limits expected to be set by IAXO. The bright yellow band indicates the prediction for the axion. Figure sourced from [18].

.

1.5.1 Light Shining Through Walls (LSW) Searches

LSW experiments are intended to produce and detect ALPs in the laboratory by sending photons from a laser source parallel to a strong magnetic field towards a blocking wall, during which they can convert into ALPs. These ALPs might subsequently reconvert into photons, once again in the presence of a strong magnetic field on the other side of the wall [18]. These reconverted photons are susceptible to detection. Figure 4 is a schematic representation of the setup of such an experiment [20].

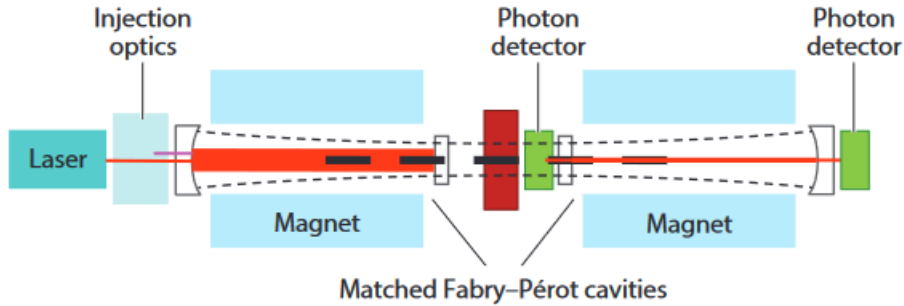Figure 4: Schematic of the setup of a Light Shining Through Walls (LSW) experiment, which involves the mixing of photons with axions, following which the axions are reconverted into photons on the other side of an optical barrier. Figure sourced from [20].

Currently, the best sensitivity of LSW experiments has been established by the Any Light Particle Search (ALPS I) experiment located at DESY. A successor experiment,

7

known as ALPS II, has also been designed with a high-power laser system, and stronger magnets. The experiment intends to probe the ALP parameter space that is favoured by astrophysical observations. However, the ability of LSW experiments to probe other spectral ranges, particularly in the microwave and X-ray ranges are still in the early stages of development, and are unlikely to yield significant results in the foreseeable future [18].

1.5.2 Haloscope Searches

Haloscopes are designed to perform direct laboratory searches for dark matter axions and ALPs originating from the Milky Way halo. The most sensitive of these experiments aim to detect the electromagnetic power which is generated from the conversion of dark matter axions and ALPs into detectable photons. They comprise of a cavity with a constant magnetic field and an oscillating electromagnetic field which is postulated to emit axions or ALPs if certain conditions are met [21]. The optimal sensitivity is achieved on resonance, at which point the power output is proportional to a quantity known as the quality factor of the cavity. One experiment that has attained a sensitivity to probe axion dark matter is the Axion Dark Matter Experiment (ADMX). The constraints on the masses and couplings of ALPs to photons set by this experiment are indicated by the vertical green band labelled 'Haloscopes' in Figure 3 above. The figure also indicates the constraints on the same parameters set by other haloscope experiments such as those performed at the PIXIE and PRISM CMB observatories [18]. Experiments with higher sensitivities than the ADMX, named ADMX (HF) and ADMX-II, which constitutes an upgrade to the existing ADMX experiment, are also proposed in order to further probe the green regions in Figure 3 above. Further information on the status of these experiments, including details of their design and structure are detailed in [22] and [23]. There is also scope to probe other mass ranges through the recycling of available microwave cavities and magnets at accelerator laboratories [18].

1.5.3 Helioscope Searches

Helioscopes are designed to detect solar ALPs (i.e. the ALPs that are produced in the Sun). The detection occurs through the conversion of the ALPs into photons, which is facilitated by a strong magnet that is directed at the Sun. Presently, a helioscope named the International Axion Observatory (IAXO) is in operation. The structure of this experiment has been modelled largely based on its predecessor, the CERN Axion Solar Telescope (CAST), with enhancements made to the design in the form of a superconducting toroidal magnet and a larger aperture, along with a detection system comprising large X-ray telescopes as well as ultra-low background X-ray detectors, and a large, more powerful tracking system. These are intended to probe the regions labelled 'IAXO' in Figure 3 above. Further details on the design and operation of the IAXO experiment and details pertaining to a smaller scale experiment known as the BabyIAXO, can be found in Refs [20] and [24] respectively.

1.5.4 Collider Searches

As a consequence of the (inverse) Primakoff effect, described in further detail in [25], the ALP searches conducted at colliders aim to exploit the coupling of these particles to photons by examining decays that contain photons either in their initial or final states [19].

This permits a link to be established with the various other search strategies described above. Furthermore, the identification of these decays over intrinsically large hadronic backgrounds becomes simpler, thereby suggesting that collider searches provide a strong prospect for probing different regions in the $(m_a, g_{a\gamma})$ parameter space to those containing the limits set by other search methods [19].
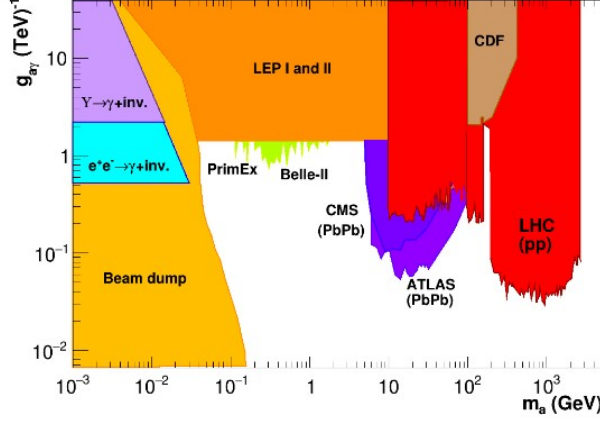
(a) Detailed bounds on the $(m_a, g_{a\gamma})$ parameter space by ALP searches from existing collider and accelerator experiments.
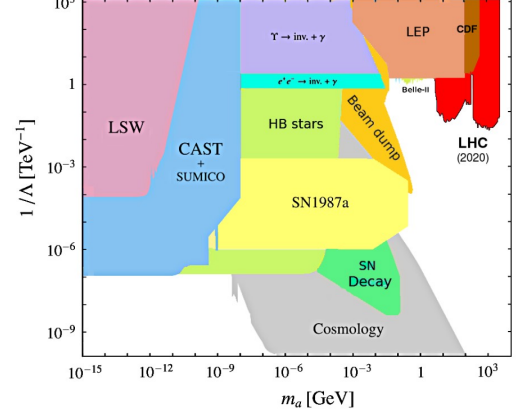
(b) Limits on $(m_a, g_{a\gamma})$ imposed by the techniques described in Section 1.5. The collider constraints in Figure 5a are also evident on the far right of this figure.

Recently, collider experiments have aimed to focus their attention on ALP masses above the MeV scale. The decay rate of $a_0 \to \gamma\gamma$ is dependent on the third power of the ALP mass, the decay rate diminishes such that the ALP leaves the detector and appears as an invisible particle as its mass increases. There also exist fixed-target proton and electron experiments wherein photons are produced by meson decays or bremsstrahlung respectively. The photons that are present in the final state of each of these processes can convert into ALPs via the Primakoff process off a nuclear target. The inverse Primakoff process is exploited when the decay mode $a_0 \to \gamma\gamma$ is probed for the presence of ALPs. Various collider experiments have aimed to constrain the masses and couplings of ALPs to photons through a multitude of decay modes, the most prominent of these being CLEO and BaBar, where mono-photon final states with missing energies from long-lived "invisible" ALPs with via radiative decays are investigated, as well as diphoton and triphoton final states, as examined by the LEP-I and LEP-II experiments via, for instance, the decay mode $e^+e^- \to \gamma a_0$ (where $a_0 \to \gamma\gamma$). Each of the experiments described above probes a different region in the $(m_a, g_{a\gamma})$ parameter space. The constraints imposed on these parameters is summarised in Figure 5a above. Figure 5b provides a more holistic perspective on the collider constraints by also including the regions of the parameter space that have been probed by the multitude of experimental techniques described above. The regions probed by the ATLAS and CMS detectors, which are sub-experiments of the Large Hadron Collider (LHC) are of particular interest, as they investigate the phenomenon in lead-lead (Pb-Pb) collisions, in contrast to the proton-proton (pp) collisions performed at the LHCb [19]

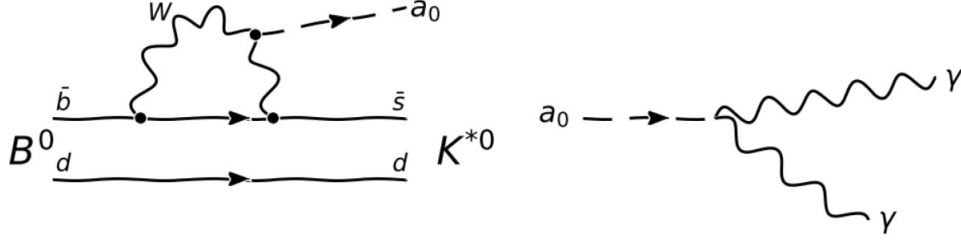## 1.6 The $B^0 \to K^* a_0, a_0 \to \gamma\gamma$ Decay Process

Figure 6: Left- One-loop level Feynman diagram of the Flavour Changing Neutral Current (FCNC) process which is responsible for the $b(\bar{b}) \to s(\bar{s})$ quark transition in the decay process described by the relation (6). This interaction takes place through the exchange of a charged W boson and is forbidden at tree-level in the Standard Model. Figure adapted from [26]. Right- Visual representation of the $a_0 \to \gamma\gamma$ decay, adapted from [10]

The model considered in the sections that follow is described in detail in [26]. The model describes a coupling to the weak gauge bosons $W^{\pm}$, which gives rise to observable signatures within the detector apparatus. This model has a zero coupling with gluons and its effective Lagrangian is given by

$$\mathcal{L} = (\partial_\mu a)^2 - \frac{1}{2}m_a^2 a^2 - \frac{g_{aW}}{4}W_{\mu\nu}\tilde{W}^{\mu\nu} \tag{5}$$

where g_{aW} is the coupling between the ALP field a and the electroweak gauge boson field W. Furthermore, $\tilde{W}^{\mu\nu} = \epsilon^{\mu\nu\alpha\beta}W_{\alpha\beta}/2$ [26].Promising decay channels which could exhibit this coupling can take place through a Flavour Changing Neutral Current (FCNC) process, further detailed in [27]. One such decay channel is

$$B^0 \to K^* a_0, a_0 \to \gamma\gamma \tag{6}$$

The above decay channel is of interest, as the decaying particle is a neutral B meson, which has been studied extensively by a multitude of accelerators and colliders that are optimised to generate and detect them. The Large Hadron Collider beauty (LHCb) is one such detector that possesses a substantial amount of data pertaining to the decay of B-mesons. For this reason, the search for ALPs that are produced by the decay channel described in (6) appears to be viable and worth pursuing at the LHCb. The design, structure, and computational framework of the experiment are further detailed in Chapter 2

1.7 Link Between ALP Mass, Coupling Strength and Branching Ratio

One can deduce a mathematical relationship between the ALP mass, m_a, its coupling strength to the W boson, and the branching ratio of the decay mode of interest for the ALP model upon which this search strategy is based (described in Section 1.6 in further

detail). The expression for the branching ratio of the $B^0 \to K^{*0}a_0, a_0 \to \gamma\gamma$ decay can be written as

$$BR(B^0 \to K^{*0}a_0, a_0 \to \gamma\gamma) = BR(B^0 \to K^{*0}a_0) \cdot BR(a_0 \to \gamma\gamma) \tag{7}$$

. Each of the terms described in Equation (7) have been related to the mass and coupling strength of the ALP to the $W^{\pm}$ bosons. The expression for the decay width, Γ, for the decay $B^0 \to K^{*0}a_0$ is given by [26]:

$$\Gamma(B^0 \to K^{*0}a_0) = \frac{M_B^3}{64\pi}|g_{abs}|^2 A_0^2(m_a^2)\lambda_{K^*a}^{3/2}, \tag{8}$$

where

$$\lambda_{K^*a} = \left[1 - \frac{(m_a + M_{K^*})^2}{M_B^2}\right]\left[1 - \frac{(m_a - M_{K^*})^2}{M_B^2}\right] \tag{9}$$

with m_a, M_B and M_{K^*} representing the masses of the ALP, the B^0, and the K^{*0} mesons respectively, and A_0^2 representing a the square of a quantity known as the form factor of the pseudoscalar current, and varies as m_a^2. Furthermore, the quantity g_{abs} represents the coupling strength of the a_0 with the b and the s quarks in the initial and final states of the decay respectively [26]. This is related to the coupling strength of the ALP to the W bosons, g_{aW} by [26]:

$$g_{abs} = -\frac{3\sqrt{2}G_F M_W^2 g_{aW}}{16\pi^2} \sum_{\alpha \in c,t} V_{\alpha b}V_{\alpha s}^* f\left(\frac{m_a^2}{M_W^2}\right) \tag{10}$$

where G_F is the Fermi constant, and $V_{\alpha b}$ and $V_{\alpha s}^*$ represent the relevant entries of the Cabibo Kobayashi Maskawa (CKM) matrix and the complex conjugates thereof respectively, noting that α is an index that pertains to the charm and top quarks, labelled c and t respectively. Furthermore, $f(x)$ is defined as [26]

$$f(x) = \frac{x[1 + x(\log(x) - 1)]}{(1 - x)^2} \tag{11}$$

Given the decay width in Equation (8), one can determine an expression for the branching ratio of the $B^0 \to K^{*0}a_0$ decay mode, which, by definition, is related to the former as

$$BR(B^0 \to K^{*0}a_0) = \Gamma(B^0 \to K^{*0}a_0)\tau_{B^0} = \frac{M_B^3}{64\pi}|g_{abs}|^2 A_0^2(m_a^2)\lambda_{K^*a}^{3/2}\tau_{B^0} \tag{12}$$

where τ_{B^0} represents the lifetime of the B^0 meson. Thus, one can obtain an expression for the first term in Equation (7) in terms of the masses of the particles that are present in the decay. A similar expression exists for the decay width of the $a_0 \to \gamma\gamma$ mode. This is given by [28]

$$\Gamma(a_0 \to \gamma\gamma) = \frac{\alpha^2 m_a^3}{4\pi\Lambda^2}|C_{\gamma\gamma}^{eff}(m_a)|^2 \tag{13}$$

Thus, the branching ratio of the $a_0 \to \gamma\gamma$ decay mode, denoted $BR(a_0 \to \gamma\gamma)$ is given by

$$BR(a_0 \to \gamma\gamma) = \Gamma(a_0 \to \gamma\gamma)\tau_{a_0} = \frac{\alpha^2 m_a^3}{4\pi\Lambda^2}|C_{\gamma\gamma}^{eff}(m_a)|^2\tau_{a_0} \tag{14}$$

where τ_{a_0} represents the lifetime of the ALP, which, for the purposes of this study, is assumed to be sufficiently short such that the ALP decays to a pair of photons that appear to originate directly from the secondary vertex (i.e. the decay vertex of the B-meson). Thus, one substitute the expressions (12) and (14) for the respective terms into Equation (7) to obtain an expression for $BR(B^0 \to K^{*0}a_0, a_0 \to \gamma\gamma)$, which, following algebraic simplification, results in:

$$BR(B^0 \to K^{*0}a_0, a_0 \to \gamma\gamma) = \left(\frac{M_B^3}{16} |g_{abs}|^2 A_0^2(m_a^2) \lambda_{K^*a_0}^{\frac{3}{2}} \right) \tau_{B^0} \left(\frac{m_a^3 \alpha}{\Lambda^2} |C_{\gamma\gamma}^{eff}|^2 \right) \tau_{a_0} \quad (15)$$

where the dependence on the coupling of the a_0 to the W boson. g_{aW} is incorporated into the g_{abs} term, as specified in Equation (10).

The relationship described by Equation (15) can be used to deduce a correlation between g_{aW} and m_a, for a fixed branching ratio, which can, in turn, be used as a metric to compare the constraints on the same that had been imposed by previous studies of the same phenomenon at other collider experiments. This is further elaborated upon in Chapter 3.

2 The LHCb Detector

2.1 Structure of the LHCb Detector

The Large Hadron Collider beauty (LHCb) detector is a single-arm spectrometer that is designed to attain a forward angular coverage ranging from 10 mrad to 300 mrad in the bending plane, and to 250 mrad in the non-bending plane [29]. The structure of the detector is motivated by the fact that both the b and the $\bar{b}$ hadrons are predominantly produced in the same forward or backward cone. The components that enable the identification of particles, and aid the deduction of their properties include the vertex locator system (VELO), the tracking system, which comprises a Trigger Tracker (a silicon microstrip detector, TT) positioned in front of the magnet, three tracking stations behind the magnet made up of silicon microstrips in the inner and outer parts (labelled IT and OT in Figure 7 respectively), two Ring Imaging Cherenkov counters (labelled RICH1 and RICH2 respectively), as well as a calorimeter system, comprising of a Scintillating Pad Detector and Preshower (SPD/PS) and electromagnetic and hadronic calorimeters (ECAL and HCAL respectively) [29]. The layout of the LHCb spectrometer including the relative positions of the components described above, is illustrated in Figure 7 below.

Of the abovementioned components, the VELO, RICH detectors, dipole magnet, and Electromagnetic Calorimeter (ECAL) play a significant role in the analysis of the decay described in Section 1.6. The structure of these components of the detector, as well as their relevance to the decay of interest is further elaborated on in the sections that follow.
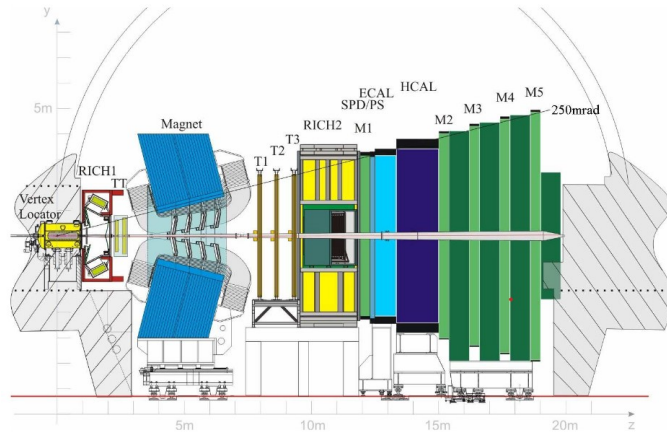
Figure 7: Diagram of the LHCb detector illustrating its various components. The coordinate system is oriented such that the beam is directed along the z axis, and the y axis is oriented along the vertical. Figure sourced from [30].

2.1.1 Vertex Locator (VELO)

The Vertex Locator (VELO) is a silicon-tracking detector in the spectrometer, positioned around the proton-proton interaction region of the LHCb experiment shown in Figure 7 above. It is responsible for the high-precision reconstruction of the primary and secondary vertices, and impact parameters of particle decays. In addition to this, it

is a key contributor to the measurements of particle lifetimes [31]. It was designed to optimise the angular coverage, triggering, reconstruction efficiency, and decay time of the resulting particles [32]. The measurements made by the VELO are a vital input to the second level trigger (L1) which enhances the b-quark decay content of the data.
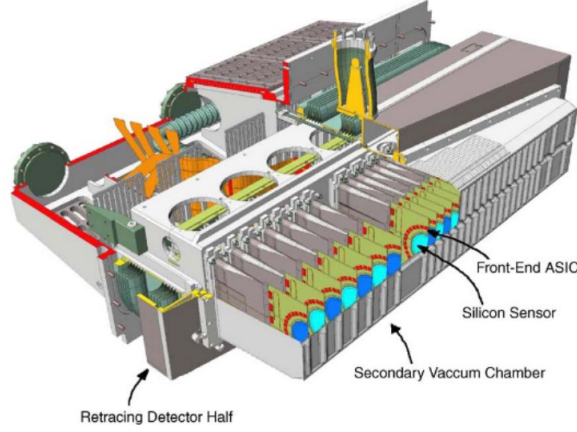

Figure 8: Diagram representing one half of the VELO detector, illustrating the locations of the silicon sensors, and the Front-End ASICs that are crucial components of each module. Figure sourced from [33].

The detector comprises 21 silicon tracking stations that are placed orthogonal to the beam direction. These are placed around and further away from the interaction point parallel to the direction of particle traversal. Each of these stations consists of two detector modules that are mounted upon independent retracting detector supports, thereby enabling the two detector halves to retract during the set-up of the colliding beams [33]. The double-sided detector modules contain two silicon sensors with different microstrip geometry, with one measuring the radial distance from the beam axis (known as the R-sensor), and the other measuring an approximate azimuthal angle, ϕ (known as the ϕ sensor) [31]. The signals from the sensors are directed out via a second metal layer to an analogue front-end ASIC. These sensors and ASICs are mounted atop a sandwich structure composed of carbon fibres and a material known as TPG (Thermalised Pyrolytic Graphite) [33]. The structure of one half of this sub-detector, including the locations of the abovementioned components is represented in Figure 8 above. Refs [32], [33], and [31] provide a more detailed overview of the various components of the VELO. In addition to this, Ref [32] presents a comprehensive account on the performance of this subdetector.

The VELO is instrumental in the study of ALPs at the LHCb experiment, as it can record information relating to the primary and secondary vertices of the decay of interest, the latter being an indicator of the point from which the ALP, as well as the final state hadrons, and photons, originate, with the former being identified by the RICH detectors, and the latter being detected by the Electromagnetic Calorimeter (ECAL).

14

2.1.2 Ring Imaging Cherenkov (RICH) Detectors

The Ring Imaging Cherenkov (RICH) system at the LHCb consists of two detectors, namely RICH1 and RICH2, and is responsible for the identification of charged hadrons (such as π, K, and p). RICH1 is placed within close proximity to the interaction region and is located immediately downstream of the VELO, described in Section 2.1.1 above. This detector is intended to cover the range of momenta from 2 to 40 GeV/c[1] over the entire angular acceptance of the spectrometer (i.e. between 25 and 300 mrad) [34]. RICH2, on the other hand, is placed downstream of the magnet, as it is intended to identify particles possessing higher momenta (i.e. between 15-100 GeV/c) over the angular range 15-120 mrad, which are less affected by the magnetic field [34].

RICH1 contains a fluorobutane (C_4F_{10}) gas radiator which provides Particle Identification (PID) for positive kaons above 2 GeV/c and π-K separation of up to 10 GeV/c. within the acceptance. The detector consists of an optical system possessing tilted spherical mirrors located in the LHCb acceptance that are traversed by charged particles and photons. The structure and materials used to construct these mirrors are elaborated upon in [35]. The Cherenkov light emitted by particles as they traverse the detector is focused onto photon detector planes by these spherical mirrors, as well as a set of secondary plane mirrors [35].Figure 9 below illustrates the layout of the RICH1 detector, with the z axis oriented to run horizontally. Further details on the structure and performance of RICH1 can be obtained in [34] and [35].
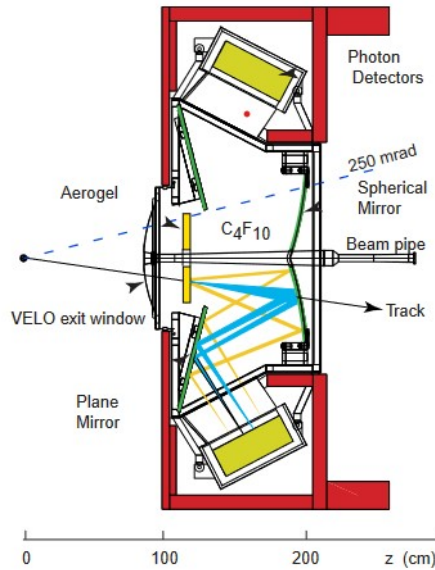
Figure 9: Layout of the vertical RICH 1 detector, depicting the spherical and the secondary plane mirrors, as well as the region containing the gas radiators. The z-axis runs horizontally in this figure, with units of cm. Figure sourced from [35].

The optical arrangement of the RICH2 detector is symmetric about the vertical plane. Much like RICH1, the detector possesses two sets of spherical and plane mirrors that

---

[1]These are known as the low and intermediate momentum regions respectively

focus Cherenkov radiation onto two photon detector arrays. CF_4 is used as the radiator material [36]. Figure 10 represents a schematic of the RICH2 detector.

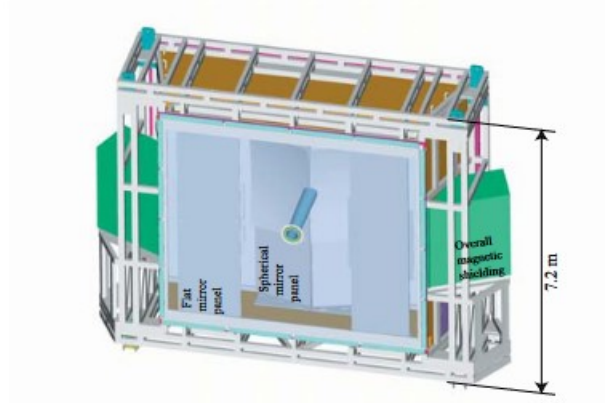Figure 10: Schematic diagram of the RICH 2 detector, depicting the overall magnetic shielding (in green), and the flat and spherical mirror panels, labelled as such. Figure sourced from [36].

The RICH detectors are relevant to this analysis as they enable the identification of the K^+ and the π^- hadrons that arise from the $K^{*0} \rightarrow K^+\pi^-$ decay. The information from this subdetector can then be utilised to infer properties of the K^{*0} meson from which these hadrons originated.

2.1.3   Magnet

The LHCb employs a magnet with a dipole field in order to measure the momenta of charged particles that traverse the detector. This measurement encompasses the forward acceptance of $\pm$ 250 mrad vertically and of $\pm$ 300 mrad horizontally. [37]. Figure 11 below depicts the layout of the magnet, including the aforementioned components and the relative scale of the structure.
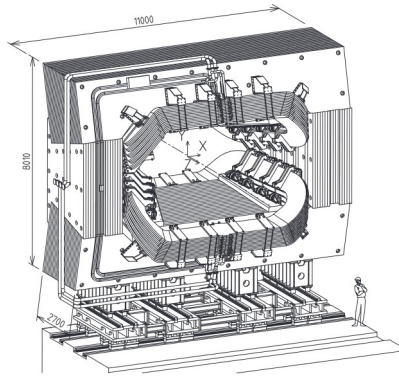

Figure 11: A perspective view of the LHCb dipole magnet with its current and water connections. The orientation of the coordinate system is also indicated on the diagram, where the units are measured in mm [38]. Figure sourced from [38].

Further information on the structure and performance of this magnet can be obtained in Refs [37], [38], and [39].

2.1.4   Electromagnetic Calorimeter (ECAL)

The ECAL is a sampling calorimeter that aims to provide precise measurements of photon energy from the shower development, so as to enable the reconstruction of B-decay modes containing either a photon or π^0 [40]. The calorimeter is constructed in a "shashlik" structure, comprising of three segmented sections, each comprising modules of an identical square size of 121.2 mm, but with varying numbers of readout cells. This 'shashlik' structure had been chosen so as to enhance the energy resolution, response time, and reliability of the calorimeter in an environment that is prone to radiation, in a cost-effective manner [41]. Each module (depicted in Figure 12a below) is comprised of alternating layers of a synthetic material made from polyethylene fibers known as Tyvek, a scintillator tile of thickness 4 mm, and a lead absorber plate of thickness 2 mm. The system possesses a total of 67 scintillator and 66 absorber layers, combining to a resultant module depth of approximately 25 radiation lengths [30]. The scintillation light is re-emitted and transported along fibres that penetrate the entire module, and is then read out with a photomultiplier tube [30].

The energy resolution, $\frac{\sigma_E}{E}$, (i.e.the accuracy of the detector in determining the energy of the incoming radiation) of the outer module of the ECAL, which consists of one cell (depicted in Figures 12a and 12b respectively) has been measured to be [40]:

$$\frac{\sigma_E}{E} = \frac{9.4\%}{\sqrt{E}} \oplus 0.8\% \tag{16}$$
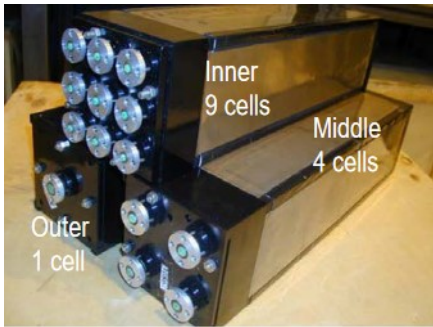
(a) The inner, middle, and outer modules of the ECAL, consisting of 9, 4 and one cells respectively. Figure sourced from [42]
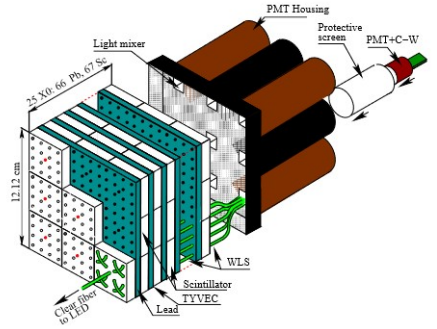
(b) Schematic diagram of an ECAL module, outlining its composition as well as the 'shashlik' structure made up of segmented sections of suitable materials. Figure sourced from [30].

The ECAL is a key component of the search for ALPs at the LHCb experiment, since it measures the energy E of the photons in the decay channel of interest (see Section 6), is a vital measurement for this analysis. The transverse energy E_T, which is a quantity of interest in the analysis can then be inferred from this measurement, as it is equivalent to

the transverse momentum, p_T of a particle with almost zero mass. The momentum of the particle of interest, p can then be inferred using this quantity. Further details on the structure and performance of the ECAL can be obtained in Refs [30], [41], and [40].

2.2 Data Analysis at the LHCb

The Large Hadron Collider supplies the LHCb with proton-proton collisions approximately 30 million times per second, thereby generating a significant amount of data [43]. In order to retain the data from events that are deemed to be of interest for analyses, the plethora of data must be filtered efficiently, and the algorithms implemented must be sufficiently intricate, so as to be able to manage the complexity of the data being processed. The LHCb experiment implements a data flow which enables the aforementioned objectives to be addressed [43]. The flow of data through the LHCb system is further detailed in the sections that follow.

2.2.1 The LHCb Data Flow

The collision events recorded by the LHCb detector proceed through various steps, each of which is controlled by an application that processes the data in a way that maximises the efficiency of data acquisition and also enhances the quality of the obtained. The data from the detector is first filtered through hardware and software components, known as the L0 trigger, and the high level trigger (HLT) respectively. Following this, the data consisting ofthe detector hits is transformed into objects such as tracks and clusters, in a process known as reconstruction. These objects are stored in an output file in a 'DST' format. Data from these files are further filtered through a set of selections known as the stripping, the output of which is produced in either a DST or a 'μDST' (micro-DST) format [43].
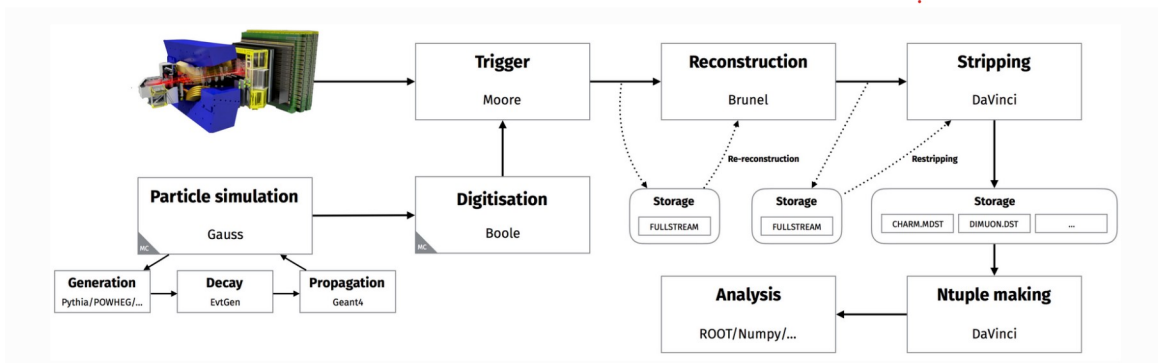
Figure 13: The LHCb Data Flow, outlining the various stages through which the data from the detector is processed, as well as the software applications responsible for the management of each stage. Figure sourced from [43].

A substantial amount of Monte Carlo (MC) simulated data is also generated in parallel to the detector data as part of the data flow. This is processed in an identical fashion to the detector data outlined above [43]. Figure 13 illustrates the abovementioned stages of the data flow and processing. The framework implemented to generate and process the simulated events described above, along with its constituent components that are

highly relevant to the analysis of the decay of interest are further elaborated upon in the subsequent sections.

2.2.2 The LHCb Simulation Framework

The MC simulated data that is processed in parallel to the detector data flows through a similar pipeline to its counterpart, with necessary steps in place to mimic the proton-proton collisions and the detector response. The Gauss application is responsible for controlling the former stage, and the subsequent hadronisation and decay of the resultant particles. Gauss is responsible for calling the multitude of available compatible Monte Carlo generators such as Pythia and POWHEG, as well as for controlling applications such as EvtGen and Geant4, which describe the decays of simulated particles and simulate their traversal through and interaction with the detector, respectively [43]. On the other hand, the latter entails the transformation of the simulated hits made in the virtual detector into signals that aim to replicate the performance of the real detector. This process is regulated by the Boole application, whose output is designed to closely match that of the real detector, such that the simulated data produced can be processed via the process described in Section 2.2.1 above. The structure of the applications that are responsible for the simulation of the proton-proton collisions (such as Gauss, EvtGen, and Geant4) are described in the following sections, as these are fundamental for performing preliminary studies to determine the viability of the search for ALPs at the LHCb.

Gauss

The Gauss application is a component of the simulation that intends to mimic the functioning and behaviour of the spectrometer to enable the understanding of the experimental conditions enforced, as well as its performance [44]. It comprises of two independent phases that are integrated and are typically run as a single job, but can be run separately if necessary. The first phase consists of the generation of proton-proton collisions (known as the event generation phase), and the decaying of the B mesons into channels that are of interest. This tool is interfaced to Pythia for the event production, and to a specialised decay package known as EvtGen (see Section 2.2.2 below). This phase also allows for the interfacing of other event generator engines if necessary.

The second phase consists of the tracking of the particles produced in the proton-proton interactions within the detector [45]. The physics processes undergone by the particles as they traverse the experimental setup are regulated by the Geant4 toolkit (see Section 2.2.2 below).

Figure 14 is a visual representation of the structure of the Gauss software that has been described above. The dependencies of the Gauss software that are relevant to this analysis, namely the Pythia, EvtGen, Geant4, and Gaudi software are further elaborated upon in the sections that follow. Further information on the architecture of the Gauss software can also be obtained in [44] and [45].
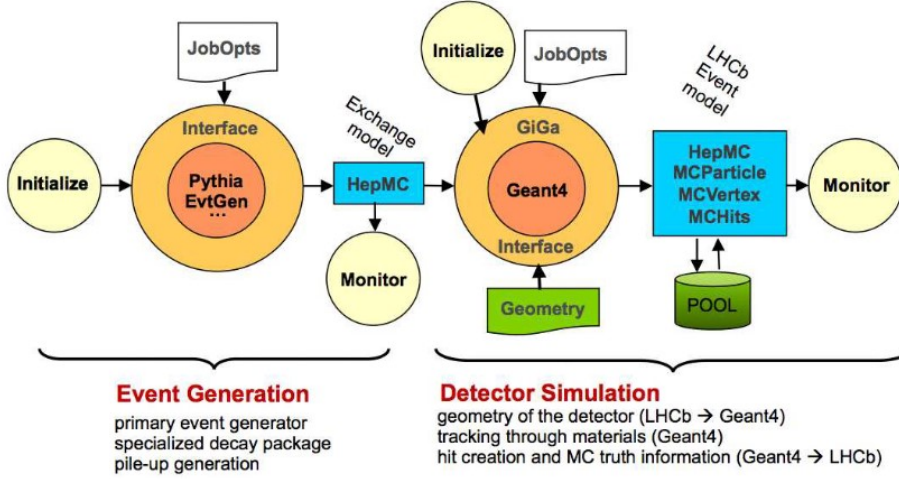
Figure 14: Visual representation of the structure of the Gauss software, depicting the Event Generation, and Detector Simulation phases, as well as the software dependencies necessary for data to be processed through these phases. Figure sourced from [45]

Pythia

The Pythia program is a standard tool for the generation of high-energy collisions [46]. The multitude of physics models implemented by the tool enable for a variety of processes, ranging from hard processes, initial and final state parton showers, multiple parton-parton interactions, and particle decays to be generated. It also possesses a set of utilities and interfaces to external programs such as, for instance, to tools that enable the calculation of Feynman rules from a Lagrangian, as well as to simulations of the detector and the subsequent analysis of the resulting data. The present version of the tool, Pythia 8, is entirely written in the C++ programming language, and currently only works with hadron-hadron and lepton-lepton collisions [46].

The internal structure of Pythia can be classified into three main parts, namely the process level, the parton level, and the hadron level [47]. Hard scattering processes and the production of resonances with short lifetimes are typically regulated by the process level, while the parton level accounts for initial and final-state radiation. At the completion of the latter stage of the event generation procedure, a realistic partonic structure, along with a description of the fundamental event is obtained. The hadron level then becomes responsible for accounting for the effects of QCD confinement of the partons produced in the previous stage. In addition to this, the hadron level is responsible for processes such as the decay of unstable hadrons. The output of this level is an event that is akin to one that can be observed in a detector. Details regarding each of the three levels described above, including the algorithms employed to generate events can be obtained in [47].

EvtGen

The EvtGen package is an event generator that is designed for the simulation of the physics of B decays. The package enables the handling of complex sequential and CP-violating

decays through the framework that it provides. The simulation of these decays proceeds using decay amplitudes instead of probabilities. The amplitude for each node in a decay is used to simulate the entire decay chain, including all angular and time-dependent correlations [48]. The computation of each decay amplitude is independent of the decay modes of the daughter particles. The package implements an algorithm that simulates correlations given individual decay amplitudes, which involves summing over the spin degrees of freedom of the daughters of the B-meson, to perform event selection. A more detailed overview of this procedure can be obtained in [48].

Geant4

The Geant4 toolkit had been developed as the basis for the simulation framework.There exist seven key domains of the simulation of the traversal of particles through matter, three of which are relevant to this analysis, namely [49]:

- Geometry and materials

- Particle interactions in matter

- Tracking management

The toolkit offers the ability to construct a geometric model with numerous components of varying shapes and materials, and is thereby responsible for the simulation of the read out electronics of the detector. Further technical details relating to the structure and dependencies of the toolkit can be obtained in [49].

Gaudi

The Gaudi framework is the architecture that serves as the link between the abovementioned dependencies of Gauss (namely Pythia, EvtGen, and Geant4). Its architecture and functionality is further elaborated upon in [50] and [51].

For the simulation of the decay mode of interest, the underlying event structure is generated by Pythia, following which the final state particles of the decay, namely the K^+ and π^- mesons that originate from the decay of the K^{*0}, as well as the photons are created from the B^0 meson by the EvtGen framework. The nature of the interactions of the K^+ and the π^- with the VELO and the tracking stations can then be deduced along with the simulation of the electromagnetic showers created in the calorimeter, both of which are performed by Geant4.

3 Analysis Methods and Experimental Status

3.1 Overview of Analysis Methods

In general, the search for, and the subsequent analysis of the $B^0 \to K^{*0}a_0, a_0 \to \gamma\gamma$ decay mode proposed in this work is based on seeking resonance structures in the invariant mass spectrum of the two photons in the final state of the decay, typically denoted $m_{\gamma\gamma}$. Such a search would be performed using events that have been selected on the basis of specific decay topologies and kinematic constraints in a process known as event selection. This process entails discriminating events on the basis of various kinematic and shape variables using an algorithm which can then be optimised using Monte Carlo (MC) simulated data that has been produced as part of the simulation framework described in Section 2.2.2. Such a process is necessary to extract only those events that contain candidates of interest. Following this, the optimised event selection algorithm can be checked for consistency using a real data sample, so as to validate that the data is accurately modelled by the MC simulation. One can then deduce an appropriate Probability Density Function (PDF) that models both the desired signal, as well as the various background contributions. The signal PDF is constructed based on MC simulated samples, while the background contributions are modelled by the real data from the high mass sideband, defined as the region in the diphoton invariant mass spectrum whose values exceed 5 GeV, and hence the probability of finding a signal in this region is highly unlikely. Once the reliability of the background model, and the consistency of the signal and background fit procedures has been validated, the signal yield can be extracted by performing a fit to this data, following which systematic errors can be estimated in order to complete the analysis.

Since the decay mode of interest has not previously been studied with data from the LHCb detector, it is necessary to conduct a preliminary analysis that determines the viability of performing the search at this experiment, prior to taking the steps described above. The remainder of this chapter provides a more detailed account of this preliminary analysis stage that has been performed by the author, and outlines the future prospects for the work that the author intends to complete as part of this study.

3.2 Preliminary Analysis

The preliminary analysis primarily entails exploring the range of limits that can be imposed on the branching ratio of the hitherto unmeasured $B^0 \to K^{*0}a_0, a_0 \to \gamma\gamma$ decay mode. From this range of limits, it is possible to determine whether this method of searching for ALPs at the LHCb through this process can impose more stringent constraints on their masses and coupling strength to photons and W bosons as outlined in the model described in Section 1.6. These projected constraints can then be compared to existing studies of the same at other collider experiments, outlined in Figure 5a. An additional study on the efficiency of the L0 electromagnetic trigger, which is responsible for the selection of decay events containing photons in their final states, was also performed in order to obtain an idea of the sensitivity of this experiment to the decay of interest, and its dependence on the mass of the ALP being considered. The details of this study have been described in the following section.

3.2.1 L0 Electromagnetic Trigger Study

As described in Section 2.2.1, the LHCb trigger system, which is responsible for the event selection process, is implemented in two key steps, consisting of the L0 trigger, which is implemented in hardware, and the software-based High Level Trigger (HLT). The L0 trigger is responsible for the selection of events containing high-energy photons, electrons, muons and hadrons. The calorimeter system, including the ECAL, as well as the HCAL, is linked to the L0 trigger system, which sums the energy deposited in the calorimeter cells, and chooses the cluster possessing the largest transverse energy. The transverse energy of a calorimeter cluster is defined as

$$E_T = \sum_{i=1}^{4} E_i \sin(\theta_i) \tag{17}$$

where E_i is the amount of energy deposited in the i-th cell, and θ_i represents the angle between the z-axis and the line from the centre of the cell to the average proton-proton interaction point [52]. The L0 photon trigger is the most relevant to the decay of interest. Hence it was necessary to investigate the efficiency of this trigger in selecting events that contain candidates of interest, and how this varies with ALP mass, as well as the transverse energy spectrum of the two final state photons in the decay denoted $E_T(\gamma\gamma)$.

In order to commence this study, we produced *generator-level* MC simulations of the $B^0 \to K^{*0}a_0, a_0 \to \gamma\gamma$ decay mode with the aid of the software described in Section 2.2.2. A generator-level simulation is one in which only the particle simulation, stripping, Ntuple making, and analysis stages of the data flow described in Figure (2.2.1) are performed [43]. A simulation of this kind has been preferred in this analysis, as opposed to a more comprehensive full detector simulation, due to the latter being significantly more time-consuming and computationally expensive, whilst containing the same essential features as the former.

Five arbitrarily chosen, different masses of the a_0, namely 0.18 GeV, 0.547 GeV, 2 GeV, 3 GeV, and 4 GeV, were simulated by the author at the generator level, with each simulation consisting of 2000 events. The lower masses of 0.18 and 0.547 GeV had been chosen in correspondence with those of the π^0 and η mesons that are produced in the topologically similar $B^0 \to K^{*0}\eta, \eta \to \gamma\gamma$, and $B^0 \to K^{*0}\pi^0, \pi^0 \to \gamma\gamma$ decays respectively. These decays, the latter in particular, are significant contributors to the irreducible background which mimics the desired signal, thereby hindering the search for the a_0 in the relevant mass regions. Nevertheless, the trigger efficiency for selecting an event containing an ALP of the said masses have been investigated in order to examine how these quantities, and $E_T(\gamma\gamma)$ (which is equivalent to the transverse momentum of the massless photons, $p_T(\gamma\gamma)$) vary with respect to one another.

The signal selection efficiency, $\varepsilon_{sel}^{\gamma\gamma}$ is defined as the percentage of photon pairs that exceed a given value of $E_T(\gamma\gamma)$. For instance, an efficiency of 80% at an $E_T(\gamma\gamma)$ of 2.5 GeV implies that 80% of the total number of simulated photons possess a transverse energy (or equivalently transverse momentum), greater than or equal to the L0 trigger threshold, for a fixed ALP mass. The L0 trigger imposes a threshold of 2.5 GeV on the transverse energy of photons produced in processes at the LHCb, meaning that only the
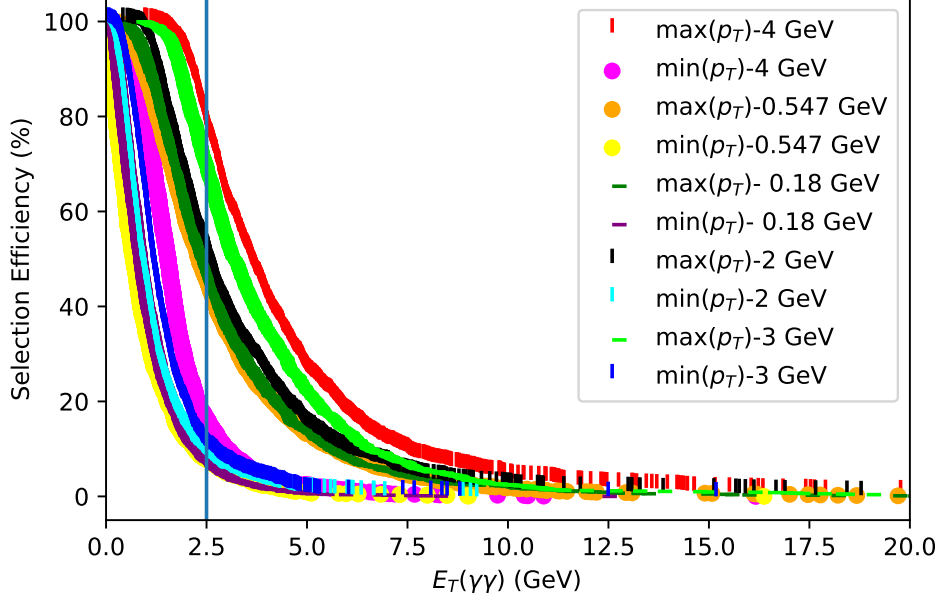
Figure 15: Plot of the signal selection efficiency as a function of the photon transverse energy for five fixed ALP masses. The curves labelled $\max(p_T)$ represent the percentage of events wherein at least one of the two photons possesses a transverse energy greater than the value specified on the horizontal axis, while those labelled $\min(p_T)$ indicate the percentage of events in which both photons exceed a given transverse energy. The L0 trigger threshold is indicated by the blue vertical line at 2.5 GeV.

events containing photons whose transverse energy exceeds 2.5 GeV are selected at the L0 level [52].In other words:

$$\varepsilon_{sel}^{\gamma\gamma} = \frac{\text{number of photon pairs that exceed a given transverse energy}}{\text{total number of generated MC events}} \times 100\% \qquad (18)$$

Figure 15 represents the variation of $\varepsilon_{sel}^{\gamma\gamma}$ with respect to $E_T(\gamma\gamma)$ for five ALP masses. The curves labelled '$\max(p_T)$' indicate the percentage of the total number of events wherein at least one of the two final state photons possesses or the transverse energy greater than or equal to that specified on the horizontal axis, while those labelled '$\min(p_T)$' signify that both of the final state photons possess a transverse energy greater than or equal to the value indicated on the horizontal axis. From the above plot, it is evident that the transverse energies (momenta) of the final state photons generally increase with an increase in ALP mass, as indicated by the upward shifts of both the $\max(p_T)$ and $\min(p_T)$ curves with an increase in the mass of the a_0, thereby indicating that a larger percentage of photons would possess a given transverse momentum for larger masses. This trend is consistent with the result expected from the conservation of four-momentum for the $a_0 \to \gamma\gamma$ decay.

Given the threshold imposed by the L0 trigger on the transverse energy of the photons, it was necessary to investigate the proportion of photon pairs whose transverse

momentum would exceed this threshold and its dependence on the mass of the ALP being considered. Figure 16 illustrates this dependence by representing the proportion of events for which at least one of the final state photons in the MC simulated data (which are identical to those used to produce Figure 15) exceeds the threshold of 2.5 GeV.

Figure 16, like Figure 15, appears to be consistent with the result obtained from the conservation of four-momentum for the $a_0 \to \gamma\gamma$ decay process. The inferences drawn from both of the above results can be used to obtain an estimate of the approximate number of signal candidates for the decay channel of interest that can be anticipated at the LHCb experiment, and may also aid the design of more optimised offline event selection algorithms that can further aid the separation of the desired signal candidates from various sources of background. The process by which the range of limits that can be imposed on the branching ratio of the $B^0 \to K^{*0}a_0, a_0 \to \gamma\gamma$ decay mode had been explored to establish the viability of this analysis is described in further detail in the section that follows.
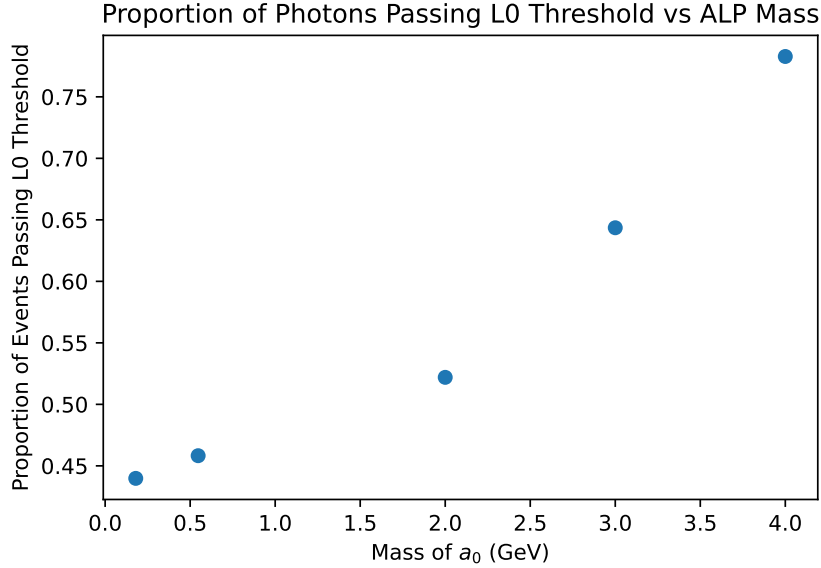

Figure 16: Proportion of events wherein at least one of the two final state photons possesses a transverse energy exceeding that of the L0 trigger threshold, as a function of ALP mass. The trend exhibited by this figure is consistent with that expected from the conservation of four-momentum of the $a_0 \to \gamma\gamma$ decay mode.

3.2.2 Bound on Branching Ratio of $B^0 \to K^{*0}a_0, a_0 \to \gamma\gamma$ Mode

In order to investigate the limits that can be applied to the branching ratio of the decay of interest, it is possible to draw a parallel to the study conducted on the topologically similar decay of the form $B^0 \to K^+\pi^-\pi^0$, which is a specific case of the more general charmless decays of the form $B^0 \to h^+h'^-\pi^0$, where h and h' can represent a variety of hadrons, as detailed in Ref [53]. This is similar to the decay of interest, as the combination of the K^+ and π^- mesons in the initial state of the former decay is analogous to the presence of the K^{*0} meson in the initial state of the decay of interest (i.e. the K^{*0} is able to decay into a K^+ and a π^-). Furthermore, the π^0 meson in the final state of the former channel can

decay into a pair of photons as $\pi^0 \to \gamma\gamma$, thus becoming comparable to the decay of interest.

The branching ratio of the $B^0 \to K^+\pi^-\pi^0$ decay mode has been measured to be $(3.6 \pm 3.0) \times 10^{-5}$ [54]. Using this measurement, along with the number of signal and background candidates that had been measured as part of the analysis of the decay outlined in [53], one can obtain an estimate for the number of signal candidates of the decay of interest that would be required to be measured to achieve a significance level of 5σ, hence providing evidence of new physics beyond the Standard Model. The limit on the branching ratio of the decay of interest can then be inferred by incorporating the abovementioned measurements into a relationship between the integrated luminosity (or the projected value thereof) of the detector at the times of the measurements. This process is described in further detail below.

In order to obtain an estimate for the number of signal candidates of the decay of interest, $\mathcal{N}_S$, that would correspond to a 90% confidence level upper limit, one can set the following expression, known as a Figure of Merit (FOM) to correspond to the desired significance level [55]

$$\text{FOM} = \frac{\mathcal{S}}{\sqrt{\mathcal{S} + \mathcal{N}_B}} \tag{19}$$

where $\mathcal{N}_B$ represents the number of background events that are measured (or expected to be measured) in the decay of interest. Assuming that the value of $\mathcal{N}_B$ for the decay of interest is identical to the number of background events measured in the analysis of the $B^0 \to K^+\pi^-\pi^0$ decay mode in Ref [53], and noting that an upper limit at the 90% confidence level corresponds to setting the FOM in Equation (19) to 1.64, one can obtain

$$1.64 = \frac{\mathcal{S}}{\sqrt{\mathcal{S} + 2475}} \tag{20}$$

Solving Equation (20) for $\mathcal{S}$ yields that $\mathcal{S} \approx 85$, indicating that approximately 85 signal candidates of the decay mode of interest need to be measured in order to obtain a 90% confidence level on the upper limit of the branching ratio that is estimated, assuming that one will measure the same number of background candidates as in the case of the analysis presented in [53]. This value of $\mathcal{S}$, can be used to deduce an approximate upper bound on the branching ratio of the decay of interest as described below.

The relationship between the integrated luminosities (denoted $\mathcal{L}$), branching ratios (denoted BR), and the number of signal candidates (labelled $\mathcal{S}$) that have been (or can be) observed for each of the decay modes described above can be written as

$$\mathcal{S}_{B^0 \to K^{*0}a_0, a_0 \to \gamma\gamma} = \frac{\mathcal{L}_{B^0 \to K^{*0}a_0, a_0 \to \gamma\gamma}}{\mathcal{L}_{B^0 \to K^+\pi^-\pi^0}} \times \frac{BR(B^0 \to K^{*0}a_0, a_0 \to \gamma\gamma)}{BR(B^0 \to K^+\pi^-\pi^0)} \times \mathcal{S}_{B^0 \to K^+\pi^-\pi^0} \tag{21}$$

Noting that the analysis presented in [53] is performed at an integrated luminosity of $\mathcal{L}_{B^0 \to K^+\pi^-\pi^0} = 1.0 \text{ fb}^{-1}$, and that the expected integrated luminosity at which the analysis of interest can be performed is 9.0 fb^{-1} [56], and that $\mathcal{S}_{B^0 \to K^+\pi^-\pi^0} = 547$ [53], and substituting the remaining known values (barring uncertainties) yields

$$85 = \frac{9}{1} \times \frac{BR(B^0 \to K^{*0}a_0, a_0 \to \gamma\gamma)}{3.6 \times 10^{-5}} \times 547 \tag{22}$$

Rearranging Equation (22) for $BR(B^0 \to K^{*0}a_0, a_0 \to \gamma\gamma)$ yields

$$BR(B^0 \to K^{*0}a_0, a_0 \to \gamma\gamma) \sim \mathcal{O}(10^{-7}) \tag{23}$$

Given that the LHCb has performed analyses of rare decays with branching ratios of $\mathcal{O}(10^{-9})$, as indicated by the study of the $B_s^0 \to \mu^+\mu^-$ decay mode presented in Ref [57], the search for the decay of interest in this analysis, whose projected branching ratio (at the 90% confidence level) is of $\mathcal{O}(10^{-7})$ appears viable. Hence, one can proceed further with this study. Figure 17 represents a plot of g_{aW} versus m_a, with the dotted and dashed curves corresponding to a fixed branching ratio, while the regions shaded in grey, red and blue represent the constraints imposed on this parameter space by other collider experiments (such as the LEP). The regions that are able to be probed by the BABAR and Belle II experiments, at the specified luminosity are also indicated by the dotted orange lines. The plot also assumes that the ALP decays exclusively to a pair of photons in the final state (i.e. $BR(a_0 \to \gamma\gamma) = 1$)
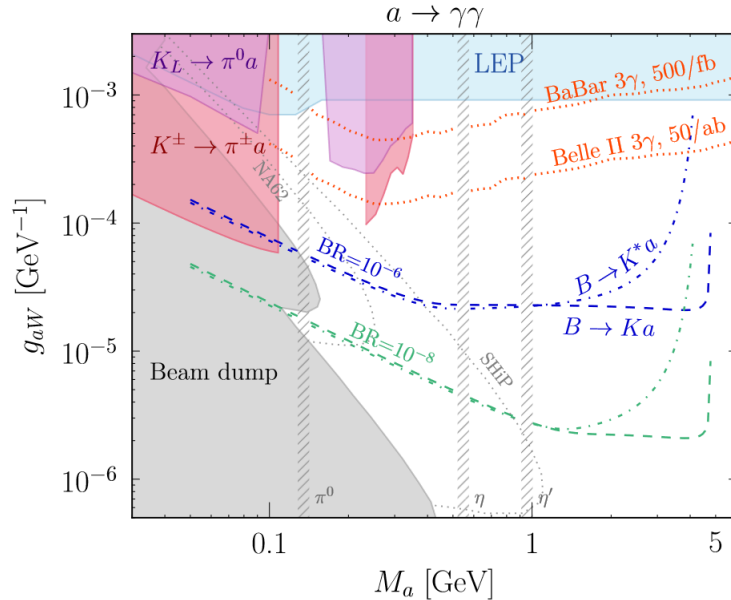

Figure 17: Plot of the coupling strength of the ALP to the $W^{\pm}$ bosons, denoted by g_{aW}, against ALP mass, m_a. The coloured regions correspond to the constraints imposed upon this parameter space by previous collider searches (e.g. LEP), while the green and blue dotted and dashed lines correspond to a fixed value of the branching ratio, labelled with the magnitude of this value. The branching ratio of the $a_0 \to \gamma\gamma$ decay mode is assumed to be equal to 1. Figure sourced from [26].

Using the limit that can be imposed upon the branching ratio of the decay $B \to K^{*0}a_0, a_0 \to \gamma\gamma$, which had been estimated in Section 3.2.2 to be $\mathcal{O}(10^{-7})$, one can visualise how g_{aW} varies as a function of m_a according to Equation (15). The curve traced by the black crosses in Figure 18 below represents the variation in these parameters corresponding to a branching ratio of $\mathcal{O}(10^{-7})$. The assumption of the a_0 decaying exclusively to two photons in its final state is present in this plot as well. The lines corresponding to the branching ratios of 10^{-6} and 10^{-8}, which also appear in Figure 17 are indicated by the

blue solid line, and the dashed orange line respectively. In addition to this, the curve corresponding to a branching ratio of $\mathcal{O}(10^{-9})$ has also been plotted as a reference, and is indicated by the graph traced by the green crosses.
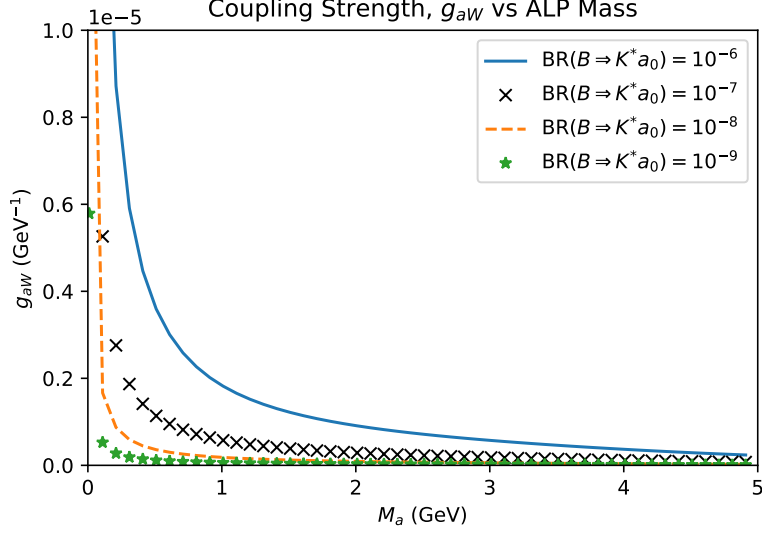

Figure 18: Plot of the strength of the ALP-$W^{\pm}$ coupling, g_{aW}, as a function of ALP mass, M_a, for a fixed branching ratio, based on the relationship described in Section (1.7). The curve corresponding to the upper limit on the branching ratio of the decay of interest at the 90% confidence level of $\mathcal{O}(10^{-7})$ is traced by the black crosses. The curves corresponding to branching ratios of $\mathcal{O}(10^{-6}), \mathcal{O}(10^{-8})$, and $\mathcal{O}(10^{-9})$ are represented by the blue, orange, and green curves respectively. Figure adapted from [26].

From the plots presented in Figures 17 and 18, it is evident that a branching ratio of $\mathcal{O}(10^{-7})$ would extend into a region of the (m_a, g_{aW}) parameter space that has hitherto not been probed by collider experiments, thereby suggesting that the prospect of searching for ALPs at the LHCb is promising, with the potential of significantly improving upon the projections made by the Belle II and BABAR experiments, as well as imposing further constraints on m_a and g_{aW} and consequently excluding more regions in the (m_a, g_{aW}) parameter space. Thus, it appears viable to proceed further with this analysis by employing the methodology described in Section 3.1.

3.3 Future Work

Given the promising outcomes of the preliminary analysis presented in the previous sections, the remainder of the procedure outlined in Section 3.1 can be followed, thereby implying that the process of event selection can be initialised for this analysis. This would entail the acquisition of full-detector MC simulated data of the decay of interest, upon which selection algorithms can be implemented and subsequently optimised. At the time of writing, the author has made requests for this data and is awaiting samples on which the analysis can commence. In addition to this, a further set of selection criteria must be applied to the data following its traversal through the trigger system, in a process known as *stripping*. In addition to this, the considerations that need to be taken pertaining to

the variation of the branching ratio of the $a_0 \to \gamma\gamma$ decay mode with respect to the ALP mass, as well as the various sources of background that could hinder the observance of the desired signal are also described in the remainder of this work.

3.3.1 Branching Ratio for $a_0 \to \gamma\gamma$

While the plots presented in Figures 17 and 18 assumed that the branching ratio of the $a_0 \to \gamma\gamma$ decay mode was equal to 1, ALPs are known to be able to decay into other (predominantly) hadronic states. The branching ratios of the various decay modes of the ALP as a function of its mass are illustrated in Figure 19. The light green curve in this Figure represents the $a_0 \to \gamma\gamma$ decay mode, which is highly dominant for smaller values of m_a, particularly those where m_a is less than twice the mass of the electron (i.e. $m_a < 2m_e$), but diminishes rapidly with an increase in m_a, as the other decay modes become dominant in this region. The dependence of this trend on the ALP model being considered remains an area of investigation at the time of writing.

The dependence of the branching ratio of the decay of the ALP on its mass is a key consideration that needs to be taken in the development of this analysis, as this could play a role in further constraining the limits that can be imposed on the (m_a, g_{aW}) or $(m_a, g_{a\gamma})$ parameter space described in Section (3.2.2).
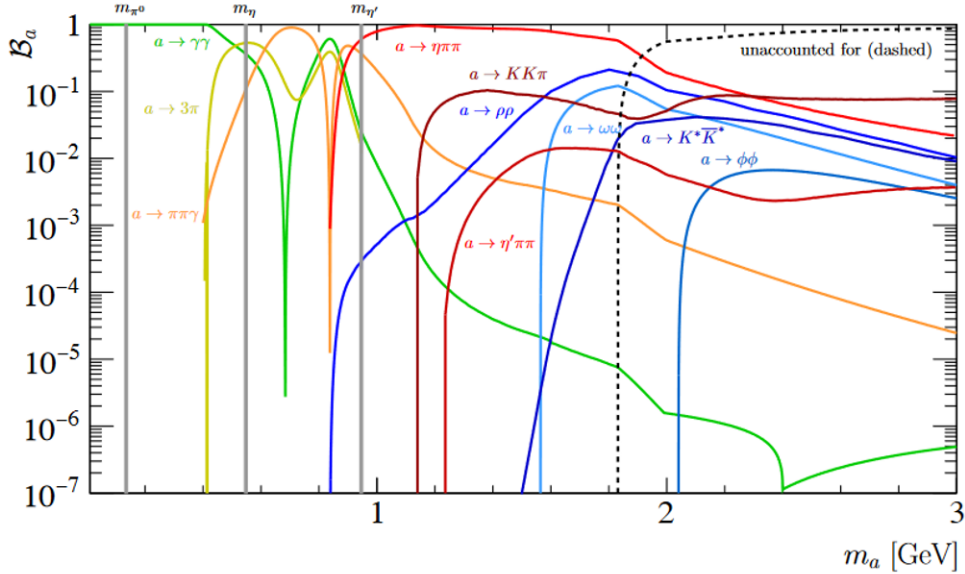

Figure 19: Plot representing the variation of the branching ratio of various possible decay modes of the a_0 with its mass. The light green curve corresponding to the $a_0 \to \gamma\gamma$ decay mode is highly dominant in the low mass regime (i.e. for $m_a < 2m_e$, where m_e represents the mass of the electron), and subsequently for larger values of m_a. Figure sourced from [34].

3.3.2 Background Sources

The significant background contributions to the mass distribution of the decay of interest can be broadly classified into two groups, namely the combinatorial background,

and the contamination from merged π^0 mesons, which are a consequence of high energy π^0 mesons produced in the $B^0 \to K^{*0}\pi^0, \pi^0\gamma\gamma$ decay mode. The small opening angle between the two photons in the final state of the decay could result in the resolution, and subsequent misidentification of these as a single photon, thereby being indistinguishable from the $B^0 \to K^{*0}\gamma$ decay mode. This effect becomes prominent once the π^0 transverse momentum exceeds 2 GeV/c. In addition to this, there also exists an *irreducible background* arising from the topologically similar decays of the form $B^0 \to K^{*0}m, m \to \gamma\gamma$, where m represents either the π^0, η, or η' mesons that necessitates the exclusion of the regions of the (m_a, g_{aW}) parameter space corresponding to the masses of these mesons, as illustrated in Figure 17. It should be noted that this analysis is oblivious to the ALPs of these masses due to the presence of this irreducible background.

Combinatorial background refers to candidates that have been reconstructed using K^+ and π^- tracks, as well as photons and pions that originated in the proton-proton collision that are not part of the decay chain of interest. This type of background is modelled using real data from the high mass sideband of the distribution of the decay, where it is certain that a signal will not be observed.

References

[1] P. Gargon, *The Standard Model: A Beautiful but Flawed Theory*, `https://shorturl.at/jvAR3`.

[2] ATLAS collaboration, G. Aad *et al.*, *Observation of a new particle in the search for the Standard Model Higgs boson with the ATLAS detector at the LHC*, Phys. Lett. B **716** (2012) 1, `arXiv:1207.7214`.

[3] B. R. Holstein, *Graviton Physics*, Am. J. Phys. **74** (2006) 1002, `arXiv:gr-qc/0607045`.

[4] I. G. Irastorza, *An Introduction to Axions and their Detection*, SciPost Physics Lecture Notes (2022) .

[5] A. D. Sakharov, *Violation of CP Invariance, C asymmetry, and Baryon Asymmetry of the universe*, Pisma Zh. Eksp. Teor. Fiz. **5** (1967) 32.

[6] J. H. Christenson, J. W. Cronin, V. L. Fitch, and R. Turlay, *Evidence for the 2π Decay of the K_2^0 Meson*, Phys. Rev. Lett. **13** (1964) 138.

[7] S. Weinberg, *A New Light Boson?*, Phys. Rev. Lett. **40** (1978) 223.

[8] U. di Barcelona, *Scientists bring us a step closer to understanding the nature of matter and antimatter*, `https://shorturl.at/mwCX5`, 2022.

[9] R. Nave, *Hyperphysics: Parity*, `https://shorturl.at/EKXZ3`, 2022.

[10] M. D. Nuccio and F. Forti, *Search for an Axion-Like Particle in B decays at the BABAR experiment and projections to the Belle II data sample*, PhD thesis, Pisa, University of Pisa, Pisa, 2018, Presented on 19 04 2018.

[11] R. D. Peccei, *The Strong CP Problem and Axions*, in *Lecture Notes in Physics*, pp. 3–17. Springer Berlin Heidelberg, 2008. doi: 10.1007/978-3-540-73518-2_1.

[12] C. Abel *et al.*, *Measurement of the Permanent Electric Dipole Moment of the Neutron*, Phys. Rev. Lett. **124** (2020) 081803.

[13] C.-T. Chan, *On the Symmetry Constraints of CP Violations in QCD*, 1997. doi: 10.48550/ARXIV.HEP-PH/9704427.

[14] R. D. Peccei and H. Quinn, *CP Conservation in the Presence of Pseudoparticles*, Physical Review Letters - PHYS REV LETT **38** (1977) 1440.

[15] A. Beekman, L. Rademaker, and J. van Wezel, *An Introduction to Spontaneous Symmetry breaking*, SciPost Physics Lecture Notes (2019) .

[16] A. Ringwald, *Exploring the Role of Axions and Other WISPs in the Dark Universe*, Phys. Dark Univ. **1** (2012) 116, `arXiv:1210.5081`.

[17] J. Isern, E. Garcí a-Berro, S. Torres, and S. Catalán, *Axions and the cooling of white dwarf stars*, The Astrophysical Journal **682** (2008) L109.

[18] A. Ringwald, *Axions and axion-like particles*, 2014. doi: 10.48550/arxiv.1407.0546.

[19] D. d'Enterria, *Collider constraints on axion-like particles*, in *Workshop on Feebly Interacting Particles*, 2021, arXiv:2102.08971.

[20] P. W. Graham *et al.*, *Experimental searches for the axion and axion-like particles*, Annual Review of Nuclear and Particle Science **65** (2015) 485, arXiv:https://doi.org/10.1146/annurev-nucl-102014-022120.

[21] P. Sikivie, *Experimental Tests of the Invisible Axion*, Phys. Rev. Lett. **51** (1983) 1415, [Erratum: Phys.Rev.Lett. 52, 695 (1984)].

[22] ADMX collaboration, R. Khatiwada *et al.*, *Axion Dark Matter Experiment: Detailed design and operations*, Rev. Sci. Instrum. **92** (2021) 124502, arXiv:2010.00169.

[23] ADMX collaboration, T. Nitta, *Operations and Data Taking Status of ADMX*, PoS **EPS-HEP2021** (2022) 180.

[24] C. Margalejo Blasco, *Status update of the axion helioscope BabyIAXO*, PoS **ICHEP2022** (2022) 113.

[25] H. Primakoff, *Photoproduction of neutral mesons in nuclear electric fields and the mean life of the neutral meson*, Phys. Rev. **81** (1951) 899.

[26] E. Izaguirre, T. Lin, and B. Shuve, *Searching for Axionlike Particles in Flavor-Changing Neutral Current Processes*, Phys. Rev. Lett. **118** (2017) 111802, arXiv:1611.09355.

[27] F. Archilli, M.-O. Bettler, P. Owen, and K. A. Petridis, *Flavour-changing neutral currents making and breaking the standard model*, Nature **546** (2017) 221.

[28] T. Ferber, A. Filimonova, R. Schäfer, and S. Westhoff, *Displaced or invisible? ALPs from B decays at Belle II*, arXiv:2201.06580.

[29] LHCb collaboration, A. A. Alves, Jr. *et al.*, *The LHCb Detector at the LHC*, JINST **3** (2008) S08005.

[30] C. Abellán Beteta *et al.*, *Calibration and performance of the LHCb calorimeters in Run 1 and 2 at the LHC*, arXiv:2008.11556.

[31] P. Kopciewicz, S. Maccolini, T. Szumlak, and on behalf of the LHCb VELO collaboration, *The LHCb vertex locator upgrade — the detector calibration overview*, Journal of Instrumentation **17** (2022) C01046.

[32] R. Aaij *et al.*, *Performance of the LHCb Vertex Locator*, Journal of Instrumentation **9** (2014) P09007.

[33] L. Eklund, *The LHCb vertex locator*, Nuclear Instruments and Methods in Physics Research Section A: Accelerators, Spectrometers, Detectors and Associated Equipment **546** (2005) 72, Proceedings of the 6th International Workshop on Radiation Imaging Detectors.

[34] LHCb RICH Group, M. Adinolfi *et al.*, *Performance of the LHCb RICH detector at the LHC*, Eur. Phys. J. C **73** (2013) 2431, `arXiv:1211.6759`.

[35] LHCb collaboration, L. Collaboration, *LHCb technical design report: Reoptimized detector design and performance*, .

[36] N. Harnew, *An overview of the status of the LHCb RICH detectors*, Nucl. Instrum. Meth. A **595** (2008) 31.

[37] LHCb collaboration, L. Collaboration, *LHCb magnet: Technical design report*, .

[38] J. Andre *et al.*, *Status of the LHCb magnet system*, IEEE Transactions on Applied Superconductivity **12** (2002) 366.

[39] J. Andre *et al.*, *Status of the LHCb dipole magnet*, IEEE Transactions on Applied Superconductivity **14** (2004) 509.

[40] A. Golutvin, *LHCb calorimetry system*, Nuclear Physics B - Proceedings Supplements **120** (2003) 258, Proceedings of the 8th International Conference on B-Physics at Hadron Machines.

[41] LHCb collaboration, L. Collaboration, *LHCb calorimeters: Technical design report*, .

[42] *CERN LHCb Calorimeter System*, `https://shorturl.at/cjNTU`.

[43] *LHCb Starterkit*, `https://shorturl.at/CLMR7`. Accessed on December 14th, 2022.

[44] L. Tlustos *et al.*, *Imaging properties of the Medipix2 system exploiting single and dual energy thresholds*, IEEE Trans. Nucl. Sci. **53** (2006) 1323.

[45] I. Belyaev *et al.*, *Handling of the generation of primary events in Gauss, the LHCb simulation framework*, Journal of Physics: Conference Series **331** (2011) 032047.

[46] T. Sjöstrand *et al.*, *An introduction to PYTHIA 8.2*, Computer Physics Communications **191** (2015) 159.

[47] C. Bierlich *et al.*, *A comprehensive guide to the physics and usage of PYTHIA 8.3*, doi: 10.21468/SciPostPhysCodeb.8 `arXiv:2203.11601`.

[48] D. J. Lange, *The EvtGen particle decay simulation package*, Nuclear Instruments and Methods in Physics Research Section A: Accelerators, Spectrometers, Detectors and Associated Equipment **462** (2001) 152, BEAUTY2000, Proceedings of the 7th Int. Conf. on B-Physics at Hadron Machines.

[49] GEANT4 collaboration, S. Agostinelli *et al.*, *GEANT4–a simulation toolkit*, Nucl. Instrum. Meth. A **506** (2003) 250.

[50] G. Barrand *et al.*, *GAUDI — A software architecture and framework for building HEP data processing applications*, Computer Physics Communications **140** (2001) 45, CHEP2000.

[51] M. Clemencic *et al.*, *Recent developments in the LHCb software framework Gaudi*, J. Phys. Conf. Ser. **219** (2010) 042006.

[52] R. Aaij *et al.*, *Design and performance of the LHCb trigger and full real-time reconstruction in run 2 of the LHC*, Journal of Instrumentation **14** (2019) P04013.

[53] D. A. Roa Romero, *Study of charmless $B_{d,s}^0 \to h^+ h'^- \pi^0$ decays in LHCb*, PhD thesis, Clermont-Ferrand U., 2013.

[54] Belle collaboration, P. Chang *et al.*, *Observation of the decays $B^0 \to K^+ \pi^- \pi^0$ and $B^0 \to \rho^- K^+$*, Phys. Lett. B **599** (2004) 148, `arXiv:hep-ex/0406075`.

[55] G. Punzi, *Sensitivity of searches for new signals and its optimization*, eConf **C030908** (2003) MODT002, `arXiv:physics/0308063`.

[56] LHCb collaboration, R. Aaij *et al.*, *Future physics potential of LHCb*, .

[57] LHCb collaboration, R. Aaij *et al.*, *Measurement of the $B_s^0 \to \mu^+ \mu^-$ decay properties and search for the $B^0 \to \mu^+ \mu^-$ and $B_s^0 \to \mu^+ \mu^- \gamma$ decays*, Phys. Rev. D **105** (2022) 012010, `arXiv:2108.09283`.